Carbon 146 (2019) 139–146

Contents lists available at ScienceDirect

Carbon

journal homepage: www.elsevier.com/locate/carbon

Interfacial failure boosts mechanical energy dissipation in carbon nanotube films under ballistic impact

Shijun Wang [a], Enlai Gao [a], Zhiping Xu [a, b, *]

[a] Applied Mechanics Laboratory, Department of Engineering Mechanics and Center for Nano and Micro Mechanics, Tsinghua University, Beijing, 100084, China

[b] Applied Mechanics and Structure Safety Key Laboratory of Sichuan Province, School of Mechanics and Engineering, Southwest Jiaotong University, Chengdu, 610031, China

ARTICLE INFO

Article history:
Received 3 December 2018
Received in revised form
29 January 2019
Accepted 31 January 2019
Available online 1 February 2019

ABSTRACT

High-performance fabrics with outstanding mechanical performance hold great promises in load-bearing and protection applications, where the capability to dissipate mechanical energy is one of the key figures of merits. We study in this work the microstructural evolution and mechanical responses of carbon nanotube films upon ballistic impact. Both cross-ply laminated and non-woven films are explored by molecular dynamics simulations, which are validated by penetration experiments. The results indicate that high stiffness and strength of carbon nanotubes offer excellent mechanical resistance. In addition to brittle fracture of the nanotubes, ductile failure of van der Waals interfaces between the nanotubes in forms of detachment or sliding opens new channels to dissipate mechanical energy resulted from the impact. The reversible nature of intertube interaction endows the film self-healable capabilities, which is superior compared to polymers that are widely used in industry, and graphene multilayers that are fractured by emitting radial cracks. Combined with the fact that carbon nanotubes feature outstanding thermal and chemical stabilities, these findings bring perceptive insights into the design of strong yet dissipative materials for load-bearing and protection applications in harsh environment.

© 2019 Published by Elsevier Ltd.

1. Introduction

Structured materials with superior mechanical resistance to loads of high strain-rates in harsh environment (e.g. high temperature, chemical attack) are highly demanded for a wide range of applications from load bearing to impact protection [1]. Efforts have been made for rational design of light-weight, impact-resistant and multi-functional materials [2–6]. Fabrics and composites of high-strength polymeric fibers such as Kevlar and ultra-high-molecular-weight polyethylene (UHWMPE) have been extensively used in impact protections. In spite of the high strength-to-weight ratio of Kevlar and UHMWPE fibers ~8 GPa/(g/cm^3) [7], the strain to failure is less than 10% under high-strain-rate loading due to the improved orientational order in these high-performance polymeric fibers [8]. Moreover, their resistance to heating and oxidization is weak. For examples, Nylon 66, spider silks and Kevlar degrade at 138 °C [9], 150 °C [10], and 450 °C [11]. Meanwhile, the mechanical performance usually decays significantly upon temperature rising, enforcing restrictions on the practical applications in harsh environment [12]. On the other hand, inorganic fibers made of ceramics, glass or metal feature higher stabilities, but relatively high mass density and low structural flexibility [13,14].

Carbon nanotubes (CNTs) based fabrics or composites are promising for impact protections thanks to their low mass density, high flexibility and excellent intrinsic mechanical, thermal, electric properties [2,15,16]. Macroscopic fibers of CNTs can be fabricated, for example, through wet spinning from well-dispersed CNT solutions [17] or solid-state assembly from as-grown CNT forests [3]. The mechanical performance of the fibers can be improved by densification, enhancing CNT alignment and minimizing microstructural defects [5]. Models have been proposed to elucidate the correlation between their microstructural complexities (porosity, bundling, entanglement, etc.) and macroscopic mechanical performance [18,19]. For fiber-woven fabrics, theories are formulated to predict energy absorption and velocity of the projectile during ballistic impact [6,20], based on which CNT films would display

* Corresponding author. Applied Mechanics Laboratory, Department of Engineering Mechanics and Center for Nano and Micro Mechanics, Tsinghua University, Beijing, 100084, China.
E-mail address: xuzp@tsinghua.edu.cn (Z. Xu).

https://doi.org/10.1016/j.carbon.2019.01.110
0008-6223/© 2019 Published by Elsevier Ltd.

outstanding performance in impact protection. To quantify this dynamical process, one can define the residual projectile speed as [6]

$$v_r = \left\{ \frac{2[E_k - E_c(t)]}{m_p + m_c/4} \right\}^{1/2} \quad (1)$$

where E_k and m_p are the incident kinetic energy and mass of the projectile, $E_c(t)$ refers to the energy of deformed (conical) films at time t, and m_c is the mass of the moving cone. The modulus-to-weight ratio of CNTs are higher than polymeric fiber by almost an order of magnitude, which results in a larger value of E_c in CNT films upon the same conical deformation with the equal weight. If the values of E_k and m_p are constants, the residual velocity v_r derived from Eq. (1) can be much lower in the CNTs-based fabrics than that in the polymeric fabrics upon same conical deformation, implying improved performance of protection [20–22]. Dynamical mechanical tests of CNT films were conducted, showing that vertically-aligned CNT films own outstanding fatigue resistance under cyclic compression with large stain [23]. Moreover, CNT films with randomly entangled network microstructures demonstrate excellent temperature-invariant viscoelasticity ranging from −196 to 1000 °C [24], holding great potential for energy absorption and dissipation applications in harsh environment. Commercial CNT sheets produced by Nanocomp Technologies, named Miralon®, are currently available for light-weight and flexible armor applications, which could reduce the weight by up to 25% in the bullet-proof vest according to ballistic tests [25]. Mechanistic studies of the microstructural evolution and mechanical responses of CNT fabrics under high-strain-rate loads or ballistic impact, however, have not been reported, prohibiting further rational design of relevant applications.

In recent studies, ballistic tests were conducted for multilayered graphene (MLG), where radial cracks are nucleated and emitted under localized impact. The high sound speed $c = (Y/\rho)^{1/2} = \sim 22.2$ km/s within the basal plane of graphene allows fast stress wave propagation [26]. The superior thermal conductivity of MLG also protects it from thermally-induced damage. Compared to the MLG with compact layer-by-layer stacking and tearing of the graphene sheets as the only route to dissipate the kinetic energy [27,28], CNT-based fabrics possess richer energy dissipation pathways by incorporating the failure of the van der Waals (vdW) interfaces between CNTs [29]. To probe the dynamical processes of mechanical energy dissipation and material failure in the CNT fabrics, we perform coarse-grained molecular dynamics (CGMD) simulations to model the microstructural evolution and mechanical responses, as well as mechanical penetration tests to characterize the failure mechanisms and validate the theoretical predictions.

2. Models and methods

2.1. Coarse-grained models for the CNT films

CG models are constructed for the CNT films as described in Ref. [4]. Rings of carbon atoms in the CNT are clustered into beads with the same mass. Two adjacent beads in a CNT are bonded by a linear spring with stiffness k_s, where $k_s = YA/r_0$ is fitted through the Young's modulus Y, cross-section area A and equilibrium inter-bead distance r_0. The strain energy for each bond under stretch is thus $E_s = k_s(r - r_0)^2/2$. Here r is the bond length after stretch. For the bending deformation of CNTs, the bead triplet is constrained by a linear angular spring with stiffness k_b, where $k_b = 2YI/r_0$ is fitted through the bending stiffness that is calculated from the Young's modulus Y and the bending moment of inertia I. The CNT breaks at a strain to failure of $\varepsilon_c = 24\%$ as predicted for armchair carbon nanotubes by full-atom MD simulations by using the Tersoff potential [30]. The strain energy of each bead triplet is $E_b = k_b(\varphi - \varphi_0)^2/2$, where φ is the angle of the triplet with an equilibrium value $\varphi_0 = \pi$. For the vdW interaction between bare CNTs in contact, the Lennard-Jones 12–6 function is used for beads located in different CNTs, that is, $E_v = 4\varepsilon[(\sigma/r)^{12} - (\sigma/r)^6]$. Here parameters ε and σ are fitted to the cohesive energy and equilibrium intertube distance, respectively. To take the interfacial friction that dissipates mechanical energies into account, Langevin thermostat is used [31]. The target temperature and damping parameter τ are set as 300 K and 10^4 fs without further specification. All parameters used in CGMD simulations are fitted to full-atom MD calculations of double-walled carbon nanotubes (DWNTs) (8, 8)/(12, 12) [4,29], which are listed in Table S1.

CG Models for the CNT films with both cross-ply laminated (CPL) and non-woven (NW) network structures are constructed (Figs. S1a and S1b). The CPL network is constructed layer by layer with a $\pi/2$ rotation for each layer and six layers are used in total. The CNTs are arranged in parallel with an equal distance that is defined by the mass density. Each CNT contains 100 beads, corresponding to an (8, 8)/(12, 12) DWNT with a length of 100 nm. Two-dimensional periodic boundary conditions (PBCs) are applied for the simulation box in the lateral (in-plane) dimensions. Consequently, for woven structures, the CNTs are continuous across the boundaries, while for non-woven structures, the CNTs are randomly placed in the simulation box, each contains two open ends. The random network is relaxed in the NVT ensemble with a Langevin thermostat at 300 K for 1 ns [29]. The final structures ensure that both the CPL and NW films have the same thickness $t = \sim 12$ nm and lateral size L.

2.2. Molecular dynamics simulations

All CGMD simulations are performed by using the large-scale atomic/molecular massively parallel simulator (LAMMPS) [32,33]. To simulate the dynamical responses of CNT films under ballistic impact, a spherical projectile is constructed based on a diamond lattice, with a diameter of $d_p = 28$ nm and a mass density of $\rho = 7.8$ g/cm^3 (Fig. 1c). The nano-projectile is constrained as a rigid body by considering the fact that the projectile in experiments is usually much stiffer than the films. We confirm that the lattice structure of a rigid projectile has negligible effects on the dynamical responses of CNT films. The interaction between the projectile and CNTs in the films is modeled through the 12-6 Lennard-Jones potential, with the same parameters for intertube interactions. As shown in Fig. 2, the projectile is initialized with a speed v_0 or constrained as v_c towards the center of CNT films.

2.3. Models and simulations for MLG and polyethylene (PE) films

A CG model is constructed for MLG through a hexagonal lattice, where the edge of triangle is modeled as an elastic spring and a pair of triangles sharing a common edge is modeled with dihedral interaction [34]. The size of a graphene layer is 100 × 100 nm, and the number of layers is between 1 and 20 in order to match the areal mass density of CNT films.

The PE is firstly modeled by full-atom MD simulations with the optimized potentials for liquid simulations (OPLS) forcefield [35]. Then a coarse-grained model is constructed based on the full-atom simulation results to perform larger-scale simulations that are comparable with the CG models of CNT and MLG films. The simulation procedure is similar to that for CNT films, and the size of model is 100 nm × 100 nm × 2 nm (Fig. S2).

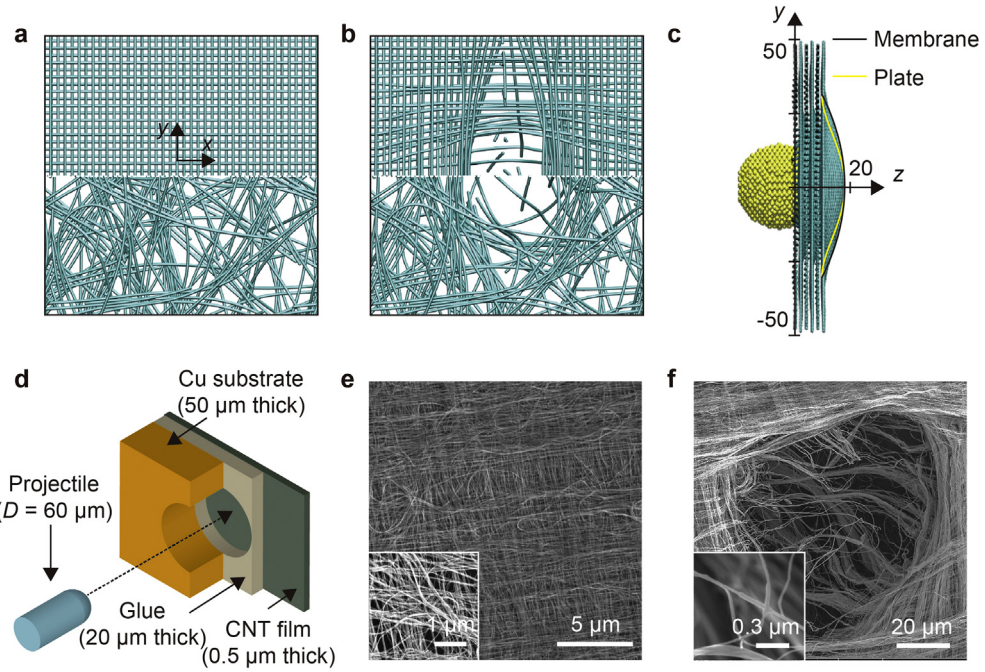

Fig. 1. (a) CPL (top half) and NW (bottom half) CNT films represented in the coarse-grained model. The length and diameter of double-walled CNTs modeled are 100 nm and 1.62 nm, and mass density of the films is 0.753 g/cm^3. The size of the simulation box (the black squares) is 100 nm × 100 nm × 15 nm, where the boundaries are fixed in simulations. (**b**) Typical fracture pattern of the CNT film after penetration. (**c**) Deformation profiles of the CPL films under ballistic impact, where the film conforms to the projectile. (**d**) The setup of mechanical penetration experiments. (**e, f**) The SEM images of thin CNT films measured before and after mechanical penetration tests, which demonstrate significant microstructural changes and a pull-out failure mode. The insets in **e, f** show the Y-type and X-type entanglement, respectively. (A colour version of this figure can be viewed online.)

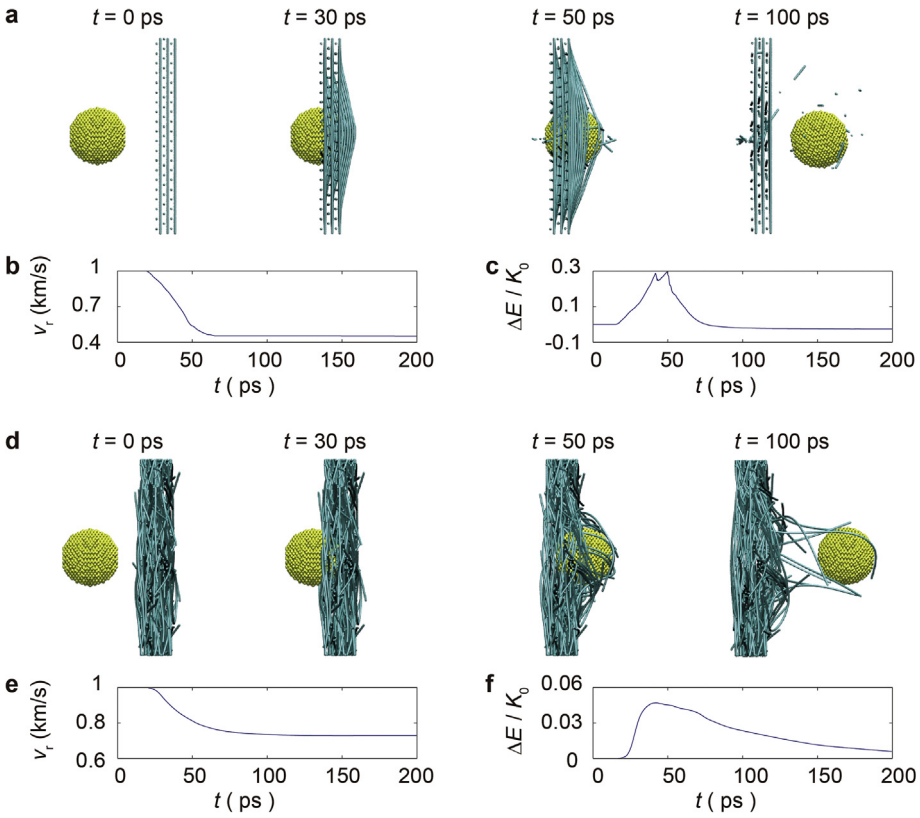

Fig. 2. Microstructural evolution and mechanical responses of CNT films under ballistic impact with an initial speed of projectile at 1 km/s (**a-c**: CPL films, **d-f**: NW films). Here v_r is the speed of projectile speed along the impact direction, and ΔE is the change in the potential energy of CNT films, measured with respect to K_0, the kinetic energy of impact. (A colour version of this figure can be viewed online.)

2.4. A continuum model for the CNT films

The continuum model for CNT film is applied for both small and large deformations of thin plates based on the Föppl-von-Karman (FvK) equations [36], which are a set of two nonlinear partial differential equations. The equations can be solved using the FEniCS-Shells package [37], where a pointwise displacement load is applied to the geometric center of films and clamping boundary conditions are enforced following the CGMD simulation setup. By varying the amplitude of displacement load z_0 and a geometric parameters D/t, the transition between the membrane and plate models is identified.

2.5. CNT film sample preparation

The CNT films are prepared by drawing sheets from a CVD-grown multiwalled CNT forest. Ten sheets are deposited on a Cu substrate (10 mm × 10 mm × 0.5 μm) layer by layer with a $\pi/2$ rotation between the neighboring layers, known as the cross-ply laminated rather than the plain-woven sheet known in the textile industry. The neat CNT sheets are then densified by dropping acetone, with the single-sheet thickness reduced from 18 μm to 50 nm [21].

2.6. Experimental penetration tests

The setup of mechanical penetration tests is illustrated in Fig. 1d, where the CNT, graphene oxide, and PE films are transferred to a Cu substrate with micro pores 1 mm in diameter using the conductive glue. A tungsten tip serves as the projectile that is forced to penetrate the films through the pores with a constant impact velocity. The diameter of the tungsten tip is 60 μm and the speed of penetration is 1 m/s. The fractured morphologies of the films are characterized using QUANTA 450 FEG scanning electron microscope (SEM).

3. Results and discussion

3.1. Modeling ballistic impact and penetration

The ballistic impact processes are studied for CPL and NW films of multiwalled CNTs (MWNTs) through CG model (Fig. 1a). Square supercells with lateral size $L = 50$, 100 and 150 nm are used, well below the persistence length of CNTs that was reported to be over 10 μm, and thus the entropic effect can be neglected [38]. The mass density ρ of the numerical models ranges from 0.25 to 1.50 g/cm^3 (0.753 g/cm^3 for the model illustrated in Fig. 2), close to values reported in the literatures (0.1, 1.39 g/cm^3) [39,40]. Two-dimensional (2D) periodic boundary conditions are used in the CGMD simulations, and the CG beads at the boundaries are fixed, representing structural supports in load-bearing or protection applications. The interactions between MWNTs are modeled through the 12-6 Lennard-Jones potential. The Langevin thermostat is used to provide the heat sink and damp excited lattice dynamics of CNTs [31]. In CPL models, CNTs are continuous across the PBCs in lateral dimensions, while in NW models, CNTs have finite lengths and free ends (Fig. 1a), and intertube sliding is activated upon loading. A projectile is initialized with a speed v_0 towards the geometrical center of films, resulting in deformation and fracture (Fig. 1b).

The size L of supercells is chosen following consideration of the computational cost, which defines a characteristic length scale, l_c, and can be scaled up through continuum mechanics analysis [41]. Simulation snapshots in Fig. 1c show that the film under impact conforms to the shape of projectile, with profiles aligning with predictions from the theory of membrane or plate, depending on the value of l_c, that is

$$z_m = z_0\left(1 - 4\frac{r^2}{D^2}\right) \text{ for a stretching} - \text{only membrane model} \tag{2}$$

and

$$z_p = z_0\left(1 - 4\frac{r^2}{D^2}\right)^2 \text{ for a bending} - \text{only plate model} \tag{3}$$

Here r is the radial coordinate measured from the film center with vertical displacement z_0. $D = \sim L$ is the size of supported region. Our CGMD simulation results (Fig. 1c) show that for $l_c = D \geq 100$ nm, the membrane model (Eq. (2)) offers a decent description. A continuum FvK model of the CNT films is constructed and solved with penetration loads [36]. To assess the applicability of plate and membrane models, we fit the scaling parameter α in

$$z = z_0\left(1 - 4\frac{r^2}{D^2}\right)^{\alpha} \tag{4}$$

from the solution of FvK calculations. The results demonstrate a membrane-plate transition in the mechanical response of CNT films, and the parameters of our simulations ($D/t = \sim$10–100, $z_0/t > 5$) correspond to the membrane limit ($\alpha = \sim$1) (Fig. S3). The understandings obtained for the submicron CG models can thus be extended to even larger scales, which are validated by penetration tests (Fig. 1d), showing that the CPL films are fractured by both breaking the CNTs and intertube sliding across the thickness direction of fabrics (Fig. 1e and f).

3.2. Failure mechanisms

To explore the effect of network topology in the CNT fabrics, we compare the mechanical responses of CPL and NW films. Simulation results show that, for the CPL films that correspond to the continuous-fiber limit, CNTs are stretched and break in the region in contact with the projectile with equibiaxial stress (Fig. 2a). With an initial value at $v_0 = 1$ km/s, the projectile is damped within 60 ps through the deformation and fracture of CNTs, with a residual speed of $v_r = 0.45$ km/s (Fig. 2b). The peaks in the evolution of potential energy profiles upon impact correspond to breaking of the CNTs (Fig. 2c). NW films with CNTs of finite lengths are less resistant to the impact due to the weak interfaces between CNTs. Moreover, microstructural changes are more spatially delocalized and more area of the film bears the load (Fig. 2d) [42,43]. The timescale of mechanical damping in NW films is similar to that of the CPL films, while the reduction in the projectile speed is less significant with $v_r = 0.72$ km/s (Fig. 2e). The potential energy profile exhibits no peaks (Fig. 2e), as the failure of NW films is established through continuous process of dissipative intertube sliding in contrast to the discrete bond-breaking events in CPL films.

We decompose the changes in potential energy of CNT films (ΔE in Fig. 2c and f) into stretching, bending and vdW components (ΔE_s, ΔE_b and ΔE_v in Fig. 3a and b). The results show that the CPL films dissipate more kinetic energies of the projectile than the NW films. In the CPL films, the change in stretching energy is dominating over the bending and vdW terms, indicating that tensile deformation and fracture of CNTs provide major impact resistance (Fig. 3a). In the CPL films, discrete peaks in the stretching energy change ΔE_s are attributed to the breakage of CNTs, while in the NW films, changes in the bending energy ΔE_b is more relevant for the energy dissipation as tension in CNTs can be released through consecutive

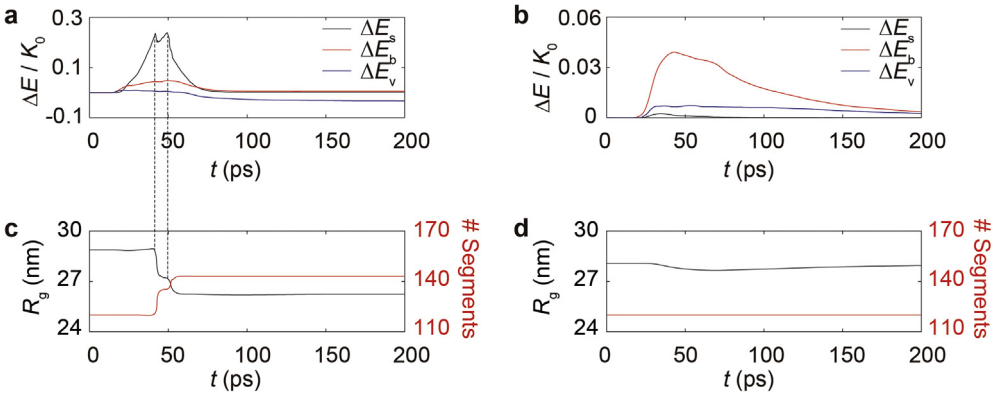

Fig. 3. (**a, b**) Mechanical energy dissipation decomposed to the stretching, bending and vdW components ΔE_s, ΔE_b and ΔE_v, measured with respect to K_0. (**c**, **d**) Time evolution of the averaged radii of gyration of individual CNTs, which measure the structural deformation of CNTs. Panels **a**, **c** and **b**, **d** are results for the CPL and NW films, respectively. (A colour version of this figure can be viewed online.)

sliding between CNTs with dissipative vdW interfaces (Fig. 3b), elevating the value of ΔE_v.

To characterize the morphological changes in the CNT networks, we calculate the radius of gyration $R_g = [\Sigma_i m_i (r_i - r_{cm})^2 / M]^{1/2}$ for individual CNTs with mass M. Here m_i and r_i are the mass and position of the i-th CG bead. r_{cm} is the center-of-mass position. Simulation results show that R_g decreases step-wisely upon impact in the CPL films before reaching a plateau, while the number of CNT segments with free/broken ends increase as well, aligning to the irreversible bond breaking events (Figs. 3c and 1b). In the NW films, CNTs are gently bent initially. The value of R_g decreases upon impact and recovers after ballistic impact, demonstrating a self-healing behavior at the intertube interfaces (Fig. 3d and S4). The change in the number of CNT fragments is not significant in our model since the load transfer between finite-length CNTs is not sufficient to break them. To quantify the microstructural recovery in CNT films, we define a degree of healability by measuring the structure through the integration of radial distribution function of the CG beads in CNTs (Figs. S4a and S4c) and the inter-tube interaction energy (Figs. S4b and S4d), which concludes that the more than 90% of the damage is healed within ~2 ns (Figs. S4e and S4f).

3.3. Protection performance

To measure the protection performance, we measure the critical speed, v_{cr}, for a projectile to penetrate the film (Fig. 4a). The CGMD simulation results show that v_{cr} increases with the density, which is controlled through the intertube or inter-fiber distance in the fabrics. The CPL film with a stretching-dominated load-bearing mechanism has much higher v_{cr} than that of the NW film. Considering the fact that the fabrication of very long CNTs is technically challenging [44], we introduce broken ends of the CNTs to model staggered CPL (SCPL) films (Fig. S1c). The value of v_{cr} decreases significantly from CPL to SCPL films, to be comparable to that of the NW films.

As a second indicator for the protection performance, the maximum resistance force (MRF) experienced by a projectile is calculated in the loading conditions with an initialized or constrained velocity (v_0 or v_c) (Fig. 4b). Simulation results with $v_0 = v_c = 1.0$ km/s show that for CPL films with $\rho < 0.8$ g/cm^3, MRFs measured under the initialized and constrained loading conditions are close, which deviate from each other as the density increases. The critical speed v_{cr} is also closely related to the film density. For CPL films, the v_{cr} is below 1.0 km/s for $\rho < 0.8$ g/cm^3, where the projectile initialized at $v_0 = 1.0$ km/s can fully penetrate the CPL films. The MRF increases as the film becomes denser, and with $\rho > 0.8$ g/cm^3, the MRF becomes independent of density, where projectiles initialized with $v_0 < v_{cr}$ (the critical speed) will be stopped by the film. The projectile constrained at v_c, however, always penetrate the film and thus the MRF increases with $\rho > 0.8$ g/cm^3. For NW and SCPL films, the values of v_{cr} are all below 1.0 km/s even at a high density $\rho = 1.5$ g/cm^3 for both initialized and constrained penetration (Fig. 4a). It should also be noted that, even though the NW films feature a similar v_c-ρ relationship with that for the SCPL films, the MRF of NW films is much lower with $\rho > 1.0$ g/cm^3.

3.4. Practical considerations for design and fabrication

The CPL and NW models represent two extremes of CNT films fabricated in practice, with long CNTs regularly patterned to bear the load cooperatively by stretching (CPL films) [29], or short CNTs randomly deposited with load carried through intertube sliding, (dis-)entanglement of their network structures (NW films). To simplify the microstructural complexity, we consider a representative volume element (RVE) (Fig. S5), where the ratio $\beta = L/l$ between the lateral span of CNT films L and the length of CNTs l is used to measure the finite-length effect. Consequently, $\beta = 1$ represents CPL films in the continuous-fiber limit, and $\beta > 1$ correspond to the SCPL and NW films, where the finite-length effect and interfacial failure become significant. The critical speed v_{cr} in CPL films is 0.92 km/s, much higher than 0.39 km/s or 0.37 km/s in NW and SCPL films with β approaches 1 (Fig. 4c), which agrees with results presented in Fig. 2b and e. Moreover, the values of v_{cr} in NW and SCPL films are close and decrease with l. These results suggest that the impact resistance is independent on microstructure as the CNTs are relatively short ($\beta > 1$). The discontinuity in the SCPL film, compared to the CPL film, may lead to stress localized in the region in contact with the projectile, especially for the SCPL films with low density and reduced vdW interaction between neighboring CNTs. The value of v_{cr} in the NW film is slightly higher than that in SCPL film for $\rho < 1.0$ g/cm^3 (Fig. 4a). Meanwhile, the layered structures in SCPL films make the interlayer sliding easy to be activated upon impact-induced conical deformation of the woven film, reducing the impact resistance. In the NW films, the interfacial interaction between CNTs is significant in the disordered but spatially uniform network, enabling load transfer and mechanical energy dissipation through the interfaces. These results suggest that we may take the advantage of 3D-woven structures to reach the load transfer and interfacial energy dissipation, to further boost the impact resistance of films [45–47]. For example, one may design a composite film with CNT bundles for high capacity of load-carrying

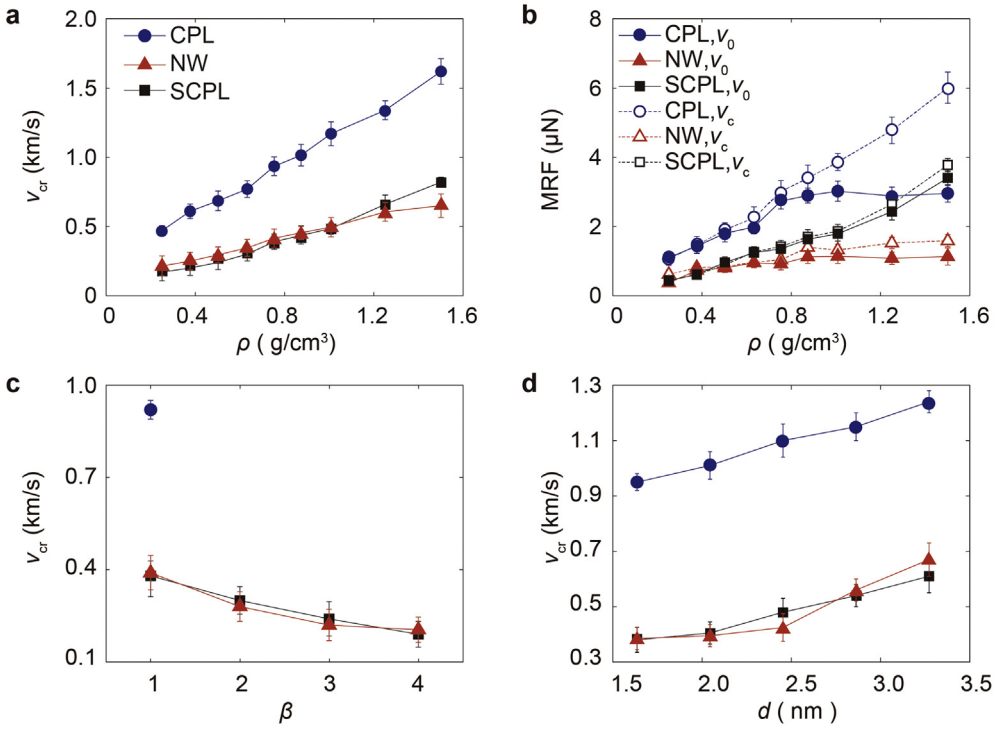

Fig. 4. (**a**) The critical speed (v_{cr}) for a projectile to penetrate the CNT film. (**b**) The maximum resistance forces (MRF) on the projectile, measured at different film densities. Here data associated with label v_0 and v_c are obtained from simulations where the projectile is set with an initial or constrained velocity of 1 km/s, respectively. (**c**, **d**) Critical speeds (v_{cr}) measured as a function of the ratio $\beta = L/l$ between the lateral span of CNT films L and the length of CNTs length l (**c**), and the diameter d of CNTs (**d**). (A colour version of this figure can be viewed online.)

interwoven by random network of CNTs for high capacity of energy dissipation.

In addition to the stretching of CNTs and intertube interaction, bending resistance of the CNTs plays a significant role in the impact resistance of NW films (Fig. 3b). Considering the CNTs as hollow cylinders composed of concentric graphitic shells, the scaling relation between the bending stiffness and the diameter is $k_b \sim d^3$ while the adhesive energy and stretching stiffness are scaled with $\varepsilon \sim d$ and $k_s \sim d$, respectively. Therefore, the critical speed v_{cr} can be modified by d as presented in Fig. 4d, where the range of the diameter can include the (8, 8)/(12, 12) ($d = 1.63$ nm) [29], (14, 0)/(16, 10) ($d = 1.78$ nm) [48], (15, 15)/(20, 20) ($d = 2.71$ nm), and (20, 20)/(25, 25) DWNTs ($d = 3.38$ nm) [49]. It should be note that, although Fig. 4d suggests that v_{cr} increases with d for CPL, NW and SCPL films with the similar amplitude. We also consider model systems with only bending stiffness of nanotubes modified ($\sim d^3$) while other parameters remain the same (Fig. S6a). The d- or k_b-dependence of v_{cr} in the model CPL films is much weaker than those in the model NW and SCPL films. Combing results in Fig. 4d and S6a, we can find that, in CPL films, the kinetic energy is mainly transferred into CNT stretching rather than dissipation through interfacial failures. On the other hand, increasing k_b only for model CPL films has a minor effect on the impact resistance, rather than the model NW and SCPL films consisting of finite-length CNTs. Microstructural heterogeneity is also considered by mixing (8, 8)/(12, 12) and (20, 20)/(25, 25) DWNTs with content ratios of 0.25/0.75, 0.50/0.50, and 0.75/0.25 (Fig. S6b), the simulation results show that the effect on dynamical mechanical resistance can be interpreted from the homogeneous counterparts. These results could advise the design of film fabrication processes, by liquid- or solid-state spinning methods [21,50,51]. In the liquid-state method, MWNTs with larger diameter remain challenges to dissolve into organic or aqueous solvents without sacrificing by damaging the CNTs [15], and thus choosing CNTs with large aspect ratios and improving their alignment could be the solution to obtain CNT films with high impact resistance. For the solid-state method, which was used to prepare samples for penetration tests in this work, controlling the alignments of the CNTs or their bundles is difficult. An inversely-proportional relation between the alignment and mean diameter of CNTs was identified in vertically self-aligned CNT arrays [52]. Consequently, using CNTs with larger diameters could be a better choice to enhance the ballistic impact resistance. CNT sheets can be drawn directly from as-grown CNT arrays, and multiple process steps can be combined for microstructural optimization and material purification [53]. Alternatively, using additive manufacturing techniques can also help to fabricate rationally-designed 3D-woven films. For example, epoxy-based ink with controlled alignment of high-aspect-ratio fibers allow the printer to create hierarchical structures [54].

3.5. Comparison with graphene and polymer films

In contrast to the CNT films, graphene and polymer films demonstrate distinct behaviors in mechanical resistance and energy dissipation (Figs. S2a and S2d). MLG films are constructed layer by layer, which fracture by nucleating radial cracks upon ballistic impact, leading usually 2–5 petals along propagation directions [26], preferentially in the armchair and zigzag directions of graphene lattices [55]. The mechanical energy dissipated thus scales with the total length of cracks, that is

$$E_d = knE_g d_p \tag{5}$$

Here k is a geometric parameter depending on the number of petals and the orientation of cracks, n is the number of graphene layers, E_g is the energy density of edge cleavage and d_p is the diameter of

projectile. In the PE film with average molecular weight of ~9300 g/mol (Fig. 5b), polymer chains are entangled, and mechanical energy is dissipated through fracture of the chains. The fracture occurs mainly in the region in contact with the projectile (Fig. S2d), and the value of E_d is proportional to the contact area. However, mechanical energy dissipation through interfaces between polymer chains is limited due to their weak resistance and topological entanglement.

In contrast, CNT films dissipate mechanical energy through fracture of CNTs or interfacial failure, which depends on the network topology. For woven CNT films with microstructural disorder, both mechanisms apply (Fig. 1e). Mechanical energy dissipated by CNT fracture is proportional to the characteristic length scale of damaged area [6], while interfacial failure can boost mechanical energy dissipation in CNT films, which scales with the total area in contact with the projectile. Our CGMD simulation results show that in CNT films, R_g is reduced by <10% only since the CNTs can be considered as elastic rods with length shorter than the persistence length. In contrast, the value of R_g in the PE films drops by ~30% (Fig. S7a) due to the shrinkage of polymer chains, leaving a hole after penetration (Fig. 5b). Although vdW interaction is relatively weaker than covalent bonding, mechanical energy dissipated through interfacial failure in the CNT films scales with the contact area and will thus be more efficient than that through radial cracks in MLGs as d_p increases. Moreover, the non-covalent, reversible nature of vdW interaction allows the recovery of CNT networks after impact within a short relaxation time of a few nanoseconds (Fig. 2). To sum up, the mechanical energy dissipation in a CNT film can be written as

$$E_d = E_{fracture} + E_{interface} = k_1 n E_{CNT} d_p + k_2 n E_{adh}\, d_p^2 \quad (6)$$

Here k_1, k_2 are geometric parameters governed by the overlap and alignment of CNTs, and n is the number of layers in the fabrics. E_{CNT} is the fracture energy density of CNTs, and E_{adh} is the adhesive energy densities between CNTs. The relationship between mechanical energy dissipation and the projectile diameter is summarized in Fig. 5c, which shows that a MLG with $n = 10$ dissipates more energy for $d_p < 40$ nm, while the NW films starts to take over as d_p further increases, at the same areal mass density. The efficiency of energy dissipation through the lattice dynamics and coupling to the environment is also important for the dynamical response, which is captured by the damping time constant, τ, of the Langevin thermostat in CGMD simulations. Our simulation results show that energy dissipation and v_{cr} decrease with τ (Fig. 5c and S7b). For the PE films, although the number of fractured bonds is also proportional to the contact area, d_p^2, the mechanical energy dissipation is much lower than that in the MLG and CNT films. The polymer chains are weaker than the graphitic walls of CNTs at the same mass density. The flexibility of PE chains results in a highly entangled network with significant energy barriers for inter-chain sliding and interfacial failure without sacrificing the covalent bonds by fracturing. Therefore, the amount of mechanical energy dissipation by interfacial failure is limited. This interpretation is consistent with the finding for NW films with reduced bending stiffness or enhanced flexibility in Fig. 4d, evidenced by a lower v_{cr} and mechanical energy dissipation.

To validate the findings offered by CGMD simulations, we performed penetration tests (see Models and Methods for details). The experimental results show that, compared to the CNT films (Fig. 1f), graphene oxide and PE films show distinct fracture patterns, agreeing well with the simulation results (Figs. 1 and 5). Three petals are identified in the graphene oxide films (Fig. S8b) [26], with similar cracks paths in all layers, which clearly indicates the tearing nature and the absence of interlayer failure (Fig. S8d). The interfacial failures are, however, commonly observed in the CNT films, which can be identified by comparing the fractured pattern (Fig. 1f) with the initial structure (Fig. 1e). In the central region of CNT films, CNT bundles break and the sheets are separated into ribbons. Intertube sliding and X- or Y-type entanglement are identified (Fig. 1f). Wavy distortion and coarsening feature of the network are identified in the damaged zone, considered as the evidences for residual deformation resulted from interfacial sliding (Fig. S8c). The self-healing behaviors of CNT films are demonstrated by reconfiguration of the random network structures after penetration (Fig. 1f), aligning with the simulation results (Figs. 2d and 3d). In the PE films, flexible polymer chains shrink and break into short fragments (Fig. 5e), leading to smooth edges after penetration (Fig. 5b).

4. Conclusion

We conducted molecular dynamics simulations and penetration experiments to explore the dynamical responses of CNT films under impact, compared with graphene and polymer films. Distinct mechanical energy dissipation mechanisms are identified, with consistent patterns of failure identified from simulations and

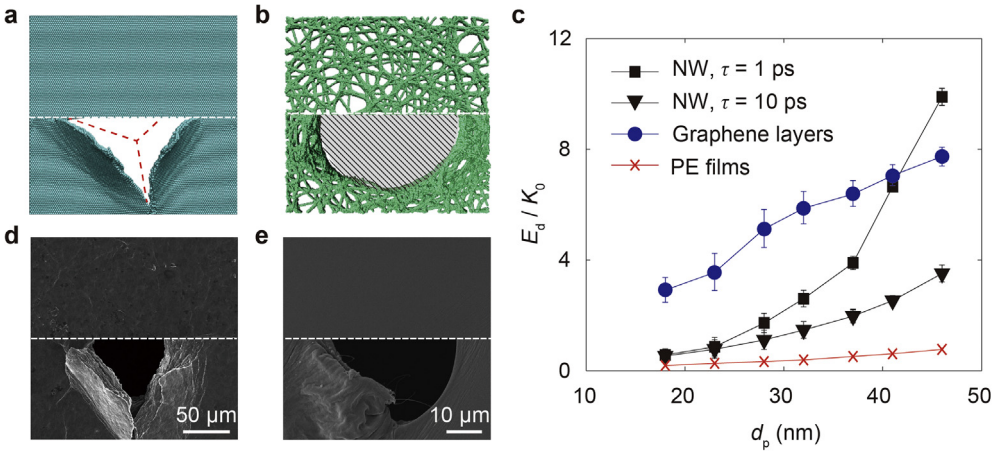

Fig. 5. Fracture patterns of (**a**) graphene and (**b**) PE films in penetration simulations. (**c**) The relationship between mechanical energy dissipation in CNT, graphene and PE films plotted as a function of the projectile diameter, where the films are 100 nm × 100 nm with the same areal mass density. Fracture patterns of (**d**) graphene oxide and (**e**) PE films in experimental penetration tests. For panels **a**, **b**, **d** and **e**, top and bottom parts are the original and fractured structures, respectively. (A colour version of this figure can be viewed online.)

penetration tests. The results show that the CNT fabric, with synergetic strong covalent bonding in the CNTs and dissipative vdW interfaces between them, is a highly promising candidate for impact resistance and protection applications, with high impact resistance and mechanical energy dissipation, as well as self-healing capabilities.

Acknowledgements

This work was supported by the Opening Project of Applied Mechanics and Structure Safety Key Laboratory of Sichuan Province through Grant SZDKF-1601, and the National Natural Science Foundation of China through Grants 11825203 and 11472150. The computation was performed on the Explorer 100 cluster system of Tsinghua National Laboratory for Information Science and Technology.

Appendix A. Supplementary data

Supplementary data to this article can be found online at https://doi.org/10.1016/j.carbon.2019.01.110.

References

[1] E.L. Thomas, Opportunities in Protection Materials Science and Technology for Future Army Applications, National Academies Press, Washington DC, 2011.
[2] R.H. Baughman, A.A. Zakhidov, W.A. de Heer, Carbon nanotubes: the route toward applications, Science 297 (2002) 787–792.
[3] M. Zhang, K.R. Atkinson, R.H. Baughman, Multifunctional carbon nanotube yarns by downsizing an ancient technology, Science 306 (2004) 1358–1361.
[4] M.J. Buehler, Nature designs tough collagen: explaining the nanostructure of collagen fibrils, Proc. Natl. Acad. Sci. U.S.A. 103 (2006) 12285–12290.
[5] H.G. Chae, S. Kumar, Making strong fibers, Science 319 (2008) 908–909.
[6] Shaktivesh, N.S. Nair, C.V.S. Kumar, N.K. Naik, Ballistic impact performance of composite targets, Mater. Des. 51 (2013) 833–846.
[7] L. Berger, H.H. Kausch, C.J.G. Plummer, Structure and deformation mechanisms in UHMWPE-fibres, Polymer 44 (2003) 5877–5884.
[8] B. Sanborn, T. Weerasooriya, Quantifying damage at multiple loading rates to Kevlar KM2 fibers due to weaving, finishing, and pre-twist, Int. J. Impact Eng. 71 (2014) 50–59.
[9] E.S. Goncalves, L. Poulsen, P.R. Ogilby, Mechanism of the temperature-dependent degradation of polyamide 66 films exposed to water, Polym. Degrad. Stabil. 92 (2007) 1977–1985.
[10] J.A. Jones, T.I. Harris, P.F. Oliveira, B.E. Bell, A. Alhabib, R.V. Lewis, Importance of heat and pressure for solubilization of recombinant spider silk proteins in aqueous solution, Int. J. Mol. Sci. 17 (2016) 1955.
[11] M. Huang, X. Li, Thermal degradation of cellulose and cellulose esters, J. Appl. Polym. Sci. 68 (1998) 293–304.
[12] H. Jiang, A.W. Wade, R.K. Eby, High performance polymer fibers, Mater. Sci. Technol. 12 (2006) 22–26.
[13] C. Zhang, H. Zhou, L. Liu, Laminar Fe-based amorphous composite coatings with enhanced bonding strength and impact resistance, Acta Mater. 72 (2014) 239–251.
[14] Z. Chen, X. Wang, V. Bhakhri, F. Giuliani, A. Atkinson, Nanoindentation of porous bulk and thin films of $La_{0.6}Sr_{0.4}Co_{0.2}Fe_{0.8}O_{3-\delta}$, Acta Mater. 61 (2013) 5720–5734.
[15] N. Behabtu, M.J. Green, M. Pasquali, Carbon nanotube-based neat fibers, Nano Today 3 (2008) 24–34.
[16] G. Otieno, A. Koos, F. Dillon, N.A. Yahya, C.E.J. Dancer, G.M. Hughes, N. Grobert, R.I. Todd, Stiffness, strength and interwall sliding in aligned and continuous multi-walled carbon nanotube/glass composite microcantilevers, Acta Mater. 100 (2015) 118–125.
[17] L.M. Ericson, H. Fan, H. Peng, V.A. Davis, W. Zhou, J. Sulpizio, Y. Wang, R. Booker, J. Vavro, C. Guthy, A.N. Parra-Vasquez, M.J. Kim, S. Ramesh, R.K. Saini, C. Kittrell, G. Lavin, H. Schmidt, W.W. Adams, W.E. Billups, M. Pasquali, W.F. Hwang, R.H. Hauge, J.E. Fischer, R.E. Smalley, Macroscopic, neat, single-walled carbon nanotube fibers, Science 305 (2004) 1447–1450.
[18] R.C. Picu, Mechanics of random fiber networks: a review, Soft Matter 7 (2011) 6768–6785.
[19] E. Gao, W. Lu, Z. Xu, Strength loss of carbon nanotube fibers explained in a three-level hierarchical model, Carbon 138 (2018) 134–142.
[20] M.R. O'Masta, D.H. Crayton, V.S. Deshpande, H.N.G. Wadley, Mechanisms of penetration in polyethylene reinforced cross-ply laminates, Int. J. Impact Eng. 86 (2015) 249–264.
[21] M. Zhang, S. Fang, A.A. Zakhidov, S.B. Lee, A.E. Aliev, C.D. Williams, K.R. Atkinson, R.H. Baughman, Strong, transparent, multifunctional, carbon nanotube sheets, Science 309 (2005) 1215–1219.
[22] Shaktivesh, N.S. Nair, N.K. Naik, Ballistic impact behavior of 2D plain weave fabric targets with multiple layers: analytical formulation, Int. J. Damage Mech. 24 (2014) 116–150.
[23] J. Suhr, P. Victor, L. Ci, S. Sreekala, X. Zhang, O. Nalamasu, P.M. Ajayan, Fatigue resistance of aligned carbon nanotube arrays under cyclic compression, Nat. Nanotechnol. 2 (2007) 417–421.
[24] M. Xu, D.N. Futaba, T. Yamada, M. Yumura, K. Hata, Carbon nanotubes with temperature-invariant viscoelasticity from -196 to 1000 ^{0}C, Science 330 (2010) 1364–1368.
[25] Nanocomp Technologies Inc., Miralon® for Armor Applications. http://www.nanocomptech.com/armor, (accessed 11/13/2018).
[26] J.H. Lee, P.E. Loya, J. Lou, E.L. Thomas, Dynamic mechanical behavior of multilayer graphene via supersonic projectile penetration, Science 346 (2014) 1092–1096.
[27] Y. Liu, B. Xie, Z. Zhang, Q. Zheng, Z. Xu, Mechanical properties of graphene papers, J. Mech. Phys. Solid. 60 (2012) 591–605.
[28] Z. Meng, A. Singh, X. Qin, S. Keten, Reduced ballistic limit velocity of graphene membranes due to cone wave reflection, Extreme Mech. Lett. 15 (2017) 70–77.
[29] B. Xie, Y. Liu, Y. Ding, Q. Zheng, Z. Xu, Mechanics of carbon nanotube networks: microstructural evolution and optimal design, Soft Matter 7 (2011) 10039–10047.
[30] J. Tersoff, Empirical interatomic potential for carbon, with applications to amorphous carbon, Phys. Rev. Lett. 61 (1988) 2879–2882.
[31] T. Schneider, E.P. Stoll, R. Morf, Brownian motion of interacting and noninteracting particles subject to a periodic potential and driven by an external field, Phys. Rev. B 18 (1978) 1417–1424.
[32] S. Plimpton, Fast parallel algorithms for short-range molecular dynamics, J. Comput. Phys. 117 (1995) 1–19.
[33] W. Zhang, J. Lin, W. Xu, H. Fu, G. Yang, SCStore: managing scientific computing packages for hybrid system with containers, Tsinghua Sci. Technol. 22 (2017) 675–681.
[34] D. Yllanes, S.S. Bhabesh, D.R. Nelson, M.J. Bowick, Thermal crumpling of perforated two-dimensional sheets, Nat. Commun. 8 (2017) 1381.
[35] W.L. Jorgensen, J. Tirado-Rives, The OPLS potential functions for proteins, energy minimizations for crystals of cyclic peptides and crambin, J. Am. Chem. Soc. 110 (1988) 1657–1666.
[36] E. Harold Mansfield, The Bending and Stretching of Plates, Cambridge University Press, New York, 1989.
[37] J.S. Hale, M. Brunetti, S.P.A. Bordas, C. Maurini, Simple and extensible plate and shell finite element models through automatic code generation tools, Comput. Struct. 209 (2018) 163–181.
[38] C.P. Broedersz, F.C. MacKintosh, Modeling semiflexible polymer networks, Rev. Mod. Phys. 86 (2014) 995–1036.
[39] L. Zhang, G. Zhang, C. Liu, S. Fan, High-density carbon nanotube buckypapers with superior transport and mechanical properties, Nano Lett. 12 (2012) 4848–4852.
[40] J. Zhao, J. Jiang, L. Wang, W. Guo, T. Rabczuk, Coarse-grained potentials of single-walled carbon nanotubes, J. Mech. Phys. Solid. 71 (2014) 197–218.
[41] Z. Song, Z. Xu, X. Huang, J. Kim, Q. Zheng, On the fracture of supported graphene under pressure, J. Appl. Mech. 80 (2013), 040911.
[42] Q. Liu, M. Li, Y. Gu, Y. Zhang, S. Wang, Q. Li, Z. Zhang, Highly aligned dense carbon nanotube sheets induced by multiple stretching and pressing, Nanoscale 6 (2014) 4338–4344.
[43] C. Wang, B. Xie, Y. Liu, Z. Xu, Mechanotunable microstructures of carbon nanotube networks, ACS Macro Lett. 1 (2012) 1176–1179.
[44] Y. Bai, R. Zhang, X. Ye, Z. Zhu, H. Xie, B. Shen, D. Cai, B. Liu, C. Zhang, Z. Jia, S. Zhang, X. Li, F. Wei, Carbon nanotube bundles with tensile strength over 80 GPa, Nat. Nanotechnol. 13 (2018) 589–595.
[45] Z. Li, B. Sun, B. Gu, FEM simulation of 3D angle-interlock woven composite under ballistic impact from unit cell approach, Comput. Mater. Sci. 49 (2010) 171–183.
[46] C. Ha-Minh, F. Boussu, T. Kanit, D. Crepin, A. Imad, Analysis on failure mechanisms of an interlock woven fabric under ballistic impact, Eng. Fail. Anal. 18 (2011) 2179–2187.
[47] B.K. Behera, B.P. Dash, Mechanical behavior of 3D woven composites, Mater. Des. 67 (2015) 261–271.
[48] A.N. Kolmogorov, V.H. Crespi, Smoothest bearings: interlayer sliding in multiwalled carbon nanotubes, Phys. Rev. Lett. 85 (2000) 4727–4730.
[49] A. Pantano, D.M. Parks, M.C. Boyce, Mechanics of deformation of single- and multi-wall carbon nanotubes, J. Mech. Phys. Solid. 52 (2004) 789–821.
[50] T.V. Sreekumar, T. Liu, S. Kumar, L.M. Ericson, R.H. Hauge, R.E. Smalley, Single-wall carbon nanotube films, Chem. Mater. 15 (2003) 175–178.
[51] Z. Wu, Z. Chen, X. Du, J.M. Logan, J. Sippel, M. Nikolou, K. Kamaras, J.R. Reynolds, D.B. Tanner, A.F. Hebard, A.G. Rinzler, Transparent, conductive carbon nanotube films, Science 305 (2004) 1273–1276.
[52] E.R. Meshot, D.W. Zwissler, N. Bui, T.R. Kuykendall, C. Wang, A. Hexemer, K.J.J. Wu, F. Fornasiero, Quantifying the hierarchical order in self-aligned carbon nanotubes from atomic to micrometer scale, ACS Nano 11 (2017) 5405–5416.
[53] R.J. Davies, C. Riekel, K.K. Koziol, J.J. Vilatela, A.H. Windle, Structural studies on carbon nanotube fibres by synchrotron radiation microdiffraction and microfluorescence, J. Appl. Crystallogr. 42 (2009) 1122–1128.
[54] B.G. Compton, J.A. Lewis, 3D-printing of lightweight cellular composites, Adv. Mater. 26 (2014) 5930–5935.
[55] K. Kim, V.I. Artyukhov, W. Regan, Y. Liu, M.F. Crommie, B.I. Yakobson, A. Zettl, Ripping graphene: preferred directions, Nano Lett. 12 (2012) 293–297.

Supporting Information for

Interfacial Failure Boosts Mechanical Energy Dissipation in Carbon Nanotube Films under Ballistic Impact

Shijun Wang[1], Enlai Gao[1] and Zhiping Xu[1,2,*]

[1]Applied Mechanics Laboratory, Department of Engineering Mechanics and Center for Nano and Micro Mechanics, Tsinghua University, Beijing 100084, China.

[2]Applied Mechanics and Structure Safety Key Laboratory of Sichuan Province, School of Mechanics and Engineering, Southwest Jiaotong University

[*]Corresponding author's email: xuzp@tsinghua.edu.cn

This *Supporting Information* material contains

I. **A List of Parameters** used in the text.

II. **Supplementary Table (S1), Figures (S1-S5) and Captions**.

I. A List of Parameters

Symbols	Variables
β	Ratio between the lateral span of CNT film and the length of CNT
L	Lateral span of CNT films
t	Thickness of CNT films
l	Length of CNT
ρ	Mass density
τ	Damping time
d	Diameter of CNTs
d_{p}	Diameter of the projectile
k_{s}	Tensile stiffness of CNTs
k_{b}	Bending stiffness of CNTs
l_c	Characteristic length
r	Radial coordinate
v_0	Initial speed of the projectile
v_{c}	Constrained speed of the projectile
v_{r}	Residual speed of the projectile
v_{cr}	Critical speed for a projectile to penetrate the film
z_0	Deflection of the films
z_{m}	Deflection from the membrane model
z_{p}	Deflection from the plate model
D	Size of supported region
ΔE	Change in potential energy
ΔE_{s}	Change in stretching energy
ΔE_{b}	Change in bending energy
ΔE_{v}	Change in van der Waals energy
E_{d}	Mechanical energy dissipation
K_0	Kinetic energy of impact
R_{g}	Radius of gyration

II. Tables, Figures and Captions

Table S1. Parameters used in the coarse-grained force field for the double-walled carbon nanotubes (8, 8)/(12, 12).

Parameters	Units	Values
Equilibrium bead distance, r_0	Å	4
Tensile stiffness, k_s	kcal mol^{-1} Å^{-2}	9.4×10^3
Equilibrium angle, φ_0	degree	180
Bending stiffness, k_b	kcal mol^{-1} rad^{-2}	4.5×10^5
12-6 Lennard-Jones parameter, ε	kcal mol^{-1}	2.724
12-6 Lennard-Jones parameter, σ	Å	18.91

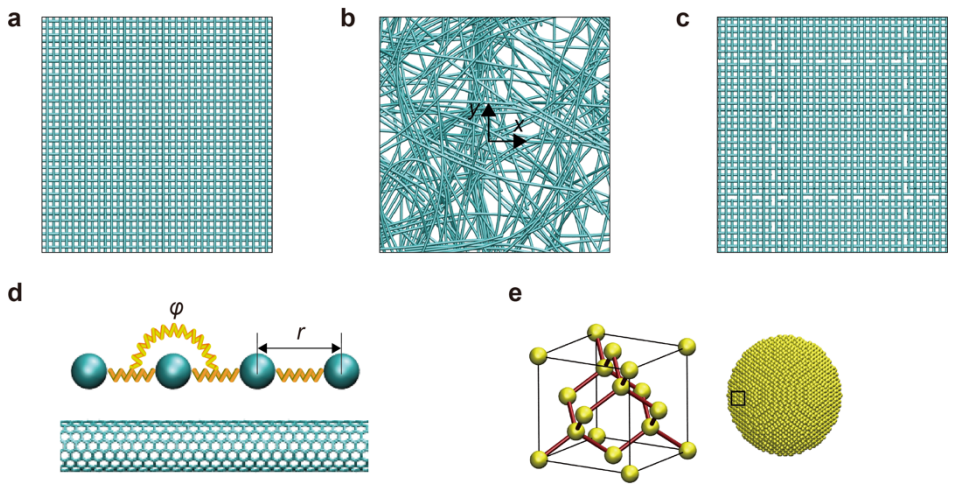

Figure S1. (a) CPL, (**b**) NW, and (**c**) SCPL CNT films represented in coarse-grained models. In the CPL structure the CNT mesh is periodic, *i.e.* in the continuous-fiber limit, while in NW structures, CNTs have finite lengths and free ends. When broken bonds are introduce to each CNT in a staggered manner in CPL films, the SCPL structures are generated. (**d**) The bead-spring triplet in the coarse-grained model for CNTs, where the spring and angle-spring constants are fitted to tensile and bending stiffness. (**e**) The coarse-grained model of projectile that is set to be rigid. The diameter is 28 nm if not further specified and the mass density is 7.8 g/cm^3.

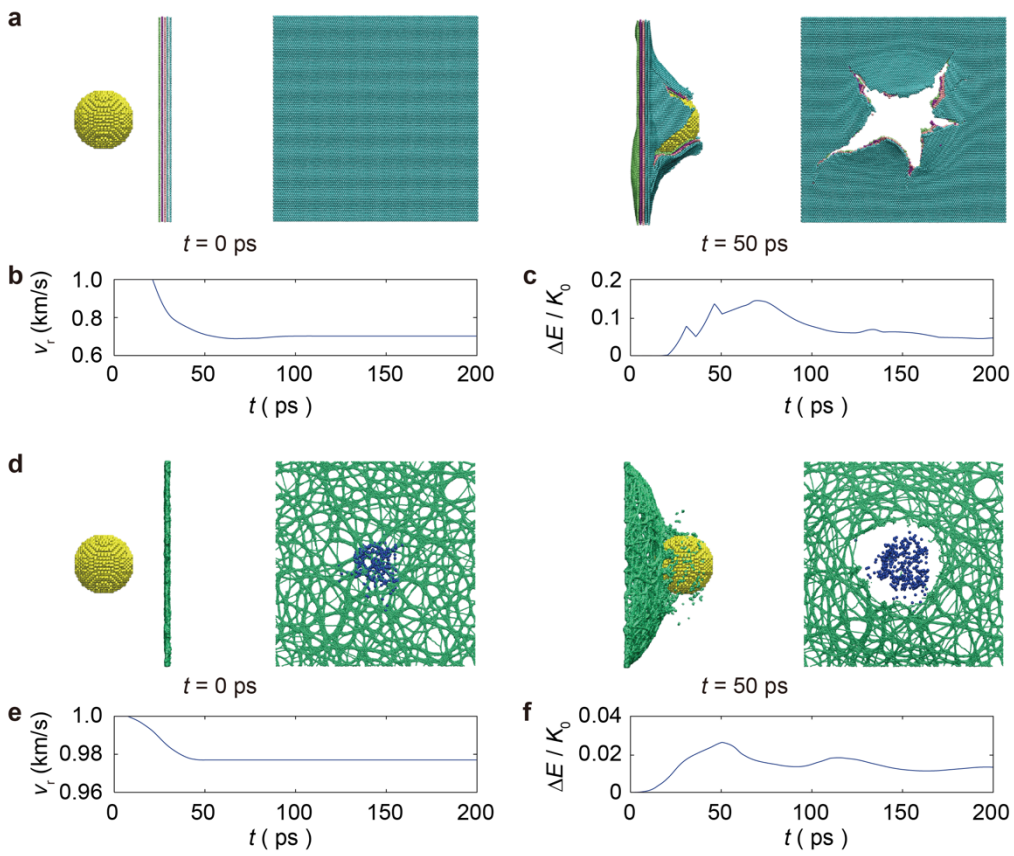

Figure S2. (**a, d**) Microstructural evolution and (**b, c, e, f**) mechanical responses of MLG and PE films under ballistic impact, obtained from CGMD simulations. The size of films is 100 nm × 100 nm and the boundaries are fixed. v_r is the residual speed of projectile and ΔE the changes in potential energy of MLG and PE films. In panel **d**, blue dots represent fractured bonds at t = 50 ps in the initial (left) and current (right) configurations.

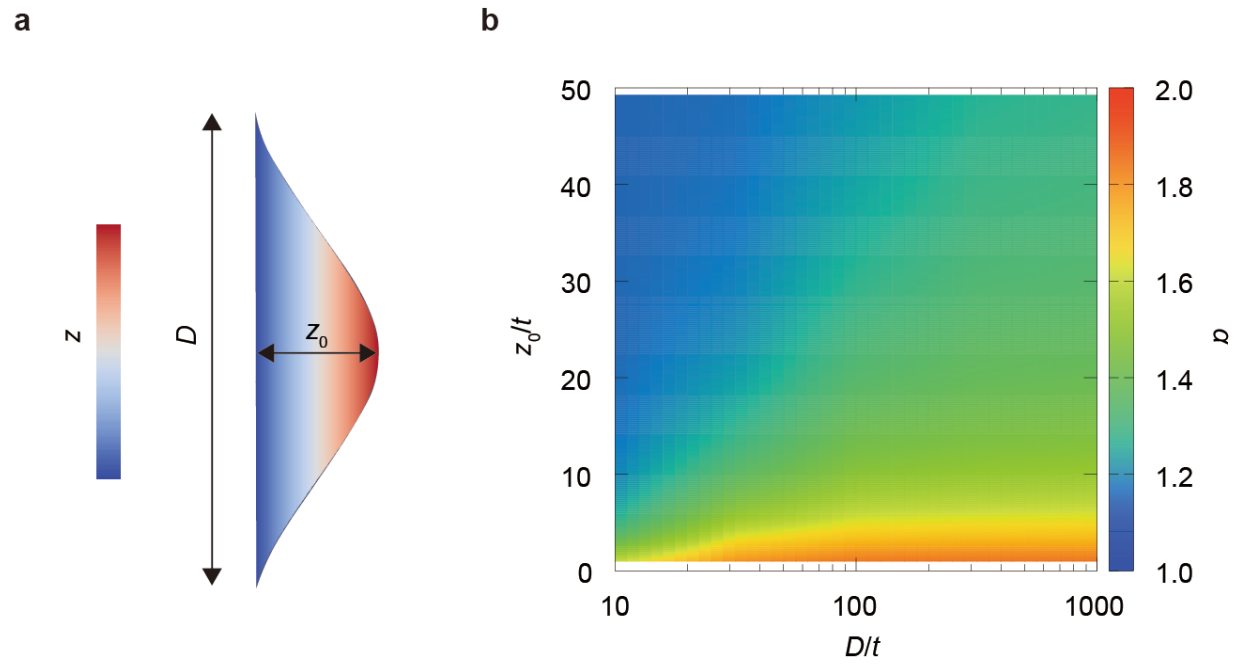

Figure S3. (a) The continuum model of CNT films under a pointwise displacement load. **(b)** The membrane-plate transition indicated by the exponential α (from 1 to 2), plotted in the space of film deflection z_0/t and geometric parameter D/t. The results show that the films considered in our CGMD simulations are in the membrane limit (α = ~1).

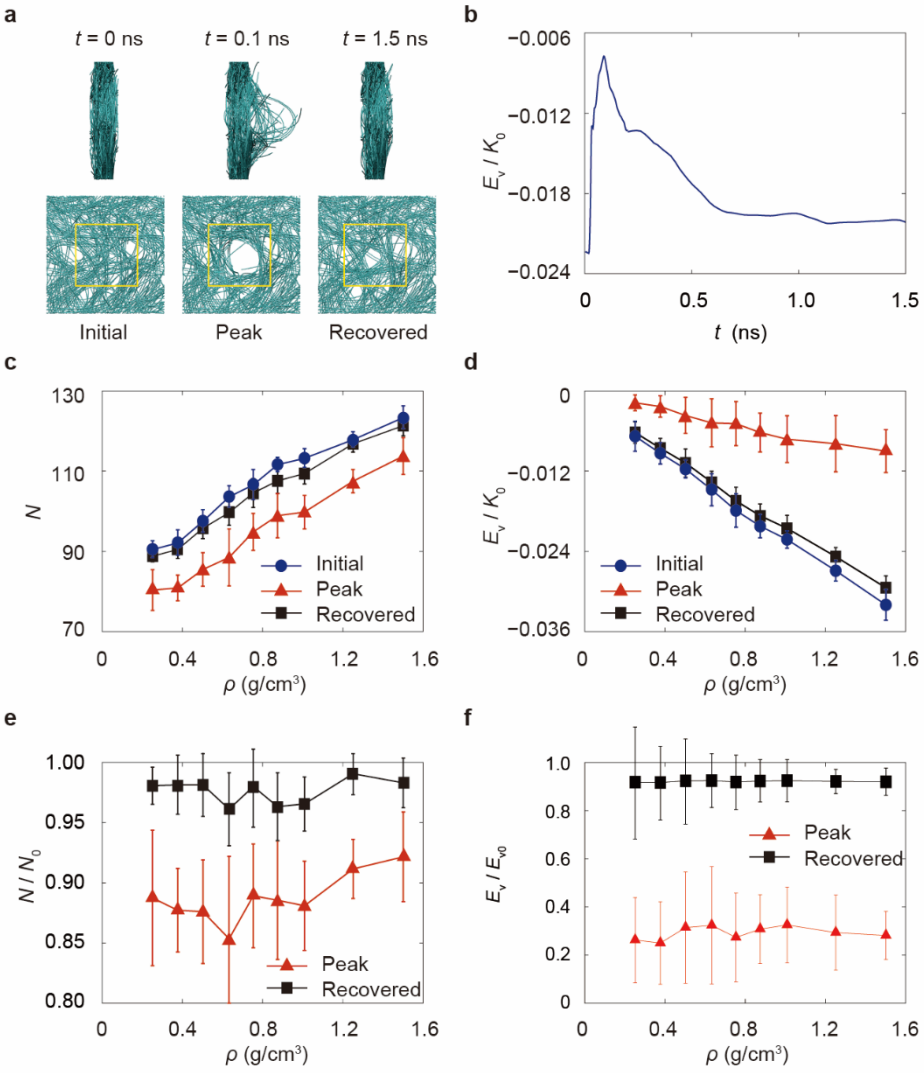

Figure S4. (**a**) Structural evolution of a NW CNT film with a density of ρ = 1.0 g/cm^3 at its initial, damage-peak, and recovered states during a ballistic test. (**b**) Evolution of the Van der Waals interaction energy between neighboring CNTs, E_v, measured with respect to K_0. (**c**) The integration, N, of the radial distribution function of the CG beads in CNTs, calculated with a cut-off of 3σ and (**d**) the van der Waals energy, E_v, calculated for NW films with different densities. All the values of N and the E_v are calculated within the region marked the yellow boxes in (**a**). Reduction of N (**e**) and E_v (**f**) in damage-peak and recovered states that are calculated with respect to the values at initial states (N_0 and E_{v0}).

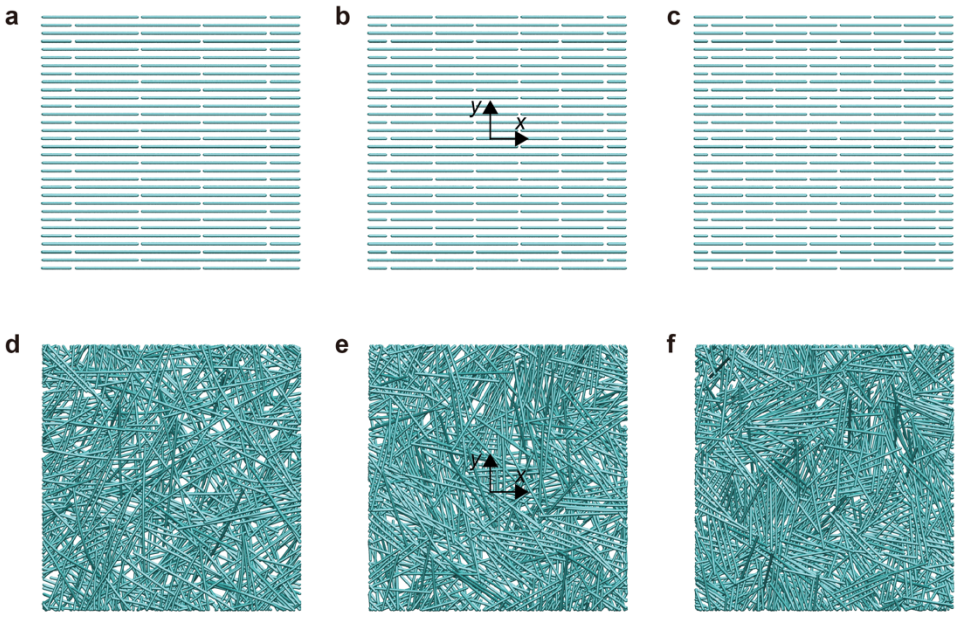

Figure S5. The top-views of RVEs of the (**a**-**c**) SCPL (one layer) and (**d**-**f**) NW films, with β = 2, 3, 4 from left to right.

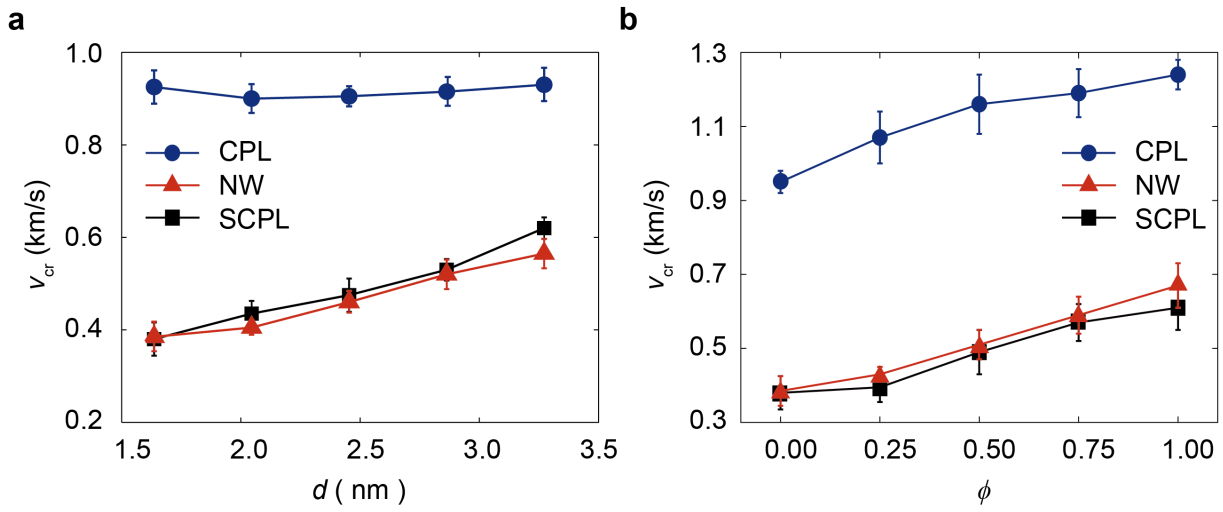

Figure S6. (**a**) The critical speed v_{cr} measured as a function of CNT diameter d, where only bending stiffness k_b is modified ($\sim d^3$) while stretching stiffness and adhesive parameters remain as the same. (**b**) The effect of the microstructural heterogeneity on the critical speed at different ratios between the number of (8, 8)/(12, 12) and (20, 20)/(25, 25) DWNTs. ϕ is the content of (20, 20)/(25, 25).

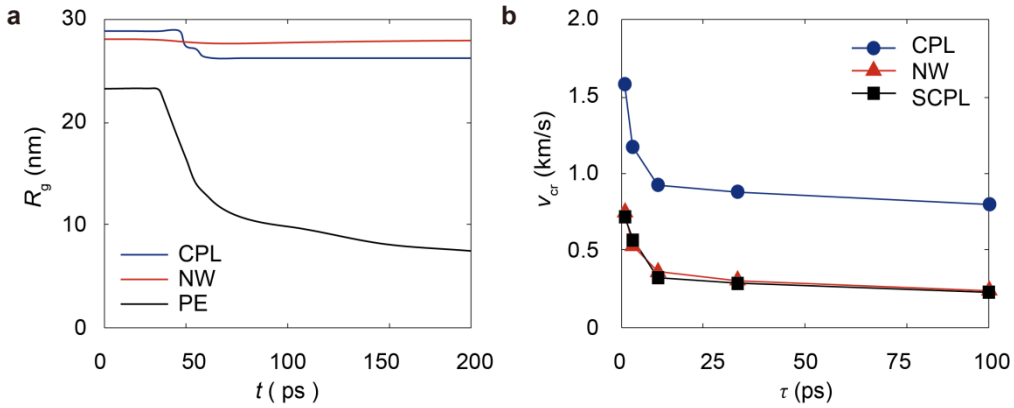

Figure S7. (**a**) Time evolution of the averaged radii of gyration of individual CNTs and PE chains in CPL, NW and PE films. (**b**) The critical speeds plotted as a function of the damping time constant τ for CPL, NW and SCPL films.

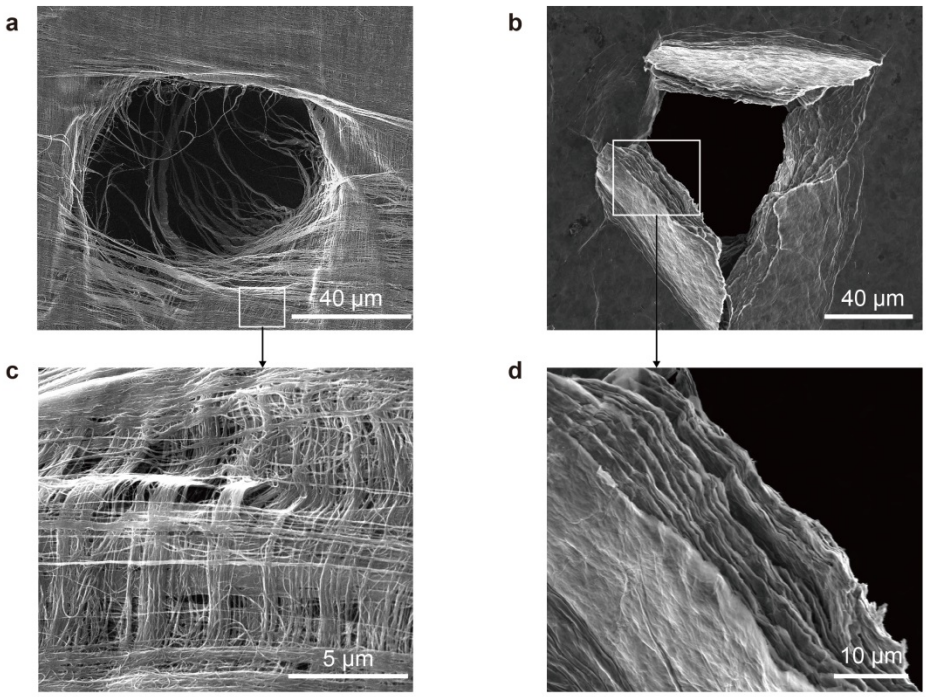

Figure S8. (**a, c**) CNT and (**b, d**) graphene oxide films after experimental penetration tests.